The 9th European Congress on Computational Methods in Applied Sciences and Engineering
ECCOMAS Congress 2024
3–7 June 2024, Lisboa, Portugal

ACTIVE CONTROL OF SEPARATED FLOW OVER A BUMP UNDER UNSTEADY AND TURBULENT CONDITIONS

HIMPU MARBONA[1,2,*], DANIEL RODRÍGUEZ[1], ALEJANDRO MARTÍNEZ-CAVA[1,3], AND EUSEBIO VALERO[1,2]

[1] Universidad Politécnica de Madrid, Plaza Cardenal Cisneros 3, E-28040 Madrid, Spain

[2]Center for Computational Simulation, Universidad Politécnica de Madrid, Campus de Montegancedo, Boadilla del Monte, 28660 Madrid, Spain

[3]Instituto Universitario "Ignacio Da Riva" (IDR/UPM), Universidad Politécnica de Madrid, Plaza Cardenal Cisneros, 3, E-28040, Madrid, Spain

[*]Corresponding author. E-mail address: himpu.marbona@upm.es

Key words: separated flow, active flow control, turbulent boundary layer, low-pressure turbine

Summary. This study investigates actuation on laminar and turbulent separation over a wall-bounded bump geometry at low Reynolds numbers. The separated flow over the bump is comparable to that observed on the suction side of low-pressure turbine blades. Actuation is introduced at the summit of the bump by modeled Zero Net Mass Flux (ZNMF) jets. Direct Numerical Simulations (DNS) are performed at various forcing frequencies and amplitudes to assess the effectiveness of the actuation strategy. The low-frequency approach targets the vortex cluster phenomenon, while the high-frequency approach is based on the Kelvin-Helmholtz frequency. Sensitivity maps are created for both laminar and turbulent cases, revealing the optimal frequency for reducing the length of the recirculation region.

1 INTRODUCTION

Low-pressure turbines (LPTs) are energy-harvesting components located near the aft end of turbofan engines. Their placement exposes them to a significant reduction in the incoming flow's Reynolds number. In a midsize turbofan engine at cruising altitude, the Reynolds number can drop as low as 100,000, based on the axial length of the blade [1], and may be even lower in high-altitude UAV engines. At these low Reynolds numbers, the boundary layer on the suction side of the LPT blades separates due to the inability to withstand the abrupt adverse pressure gradient. This separation impacts engine performance, particularly during high-altitude flight [1, 2, 3, 4]. Reducing the separation region through active control is therefore essential for improving engine efficiency [5, 6].

Assessing separated boundary layer flows typically involves applying localized adverse pressure gradients to test article sections. Two primary methods are commonly used for LPT blade research. The first method creates an artificial pressure gradient on a flat surface in a channel by using converging and diverging nozzles on the opposite side of the surface [4, 7, 8]. The second

method employs bump-shaped geometries to simulate the suction side of LPT blades or airfoils [9, 10, 11, 12, 13, 14, 15, 16]. In this study, the bump-shaped geometry is adopted based on the experimental work of Saavedra and Paniagua [11], Nowak *et al.* [14], and the numerical study by Marbona *et al.* [16].

Hourmouziadis [1] and Mayle [2] classify boundary layer separation into three distinct states. The first state is laminar separation, where the flow separates while still laminar, forming a long bubble with a substantial 'dead air' region [2]. The second state involves separation within a turbulent boundary layer, usually resulting in a shorter bubble and a larger entrainment region. The third state is an intermittent form of separation. Figure 1 illustrates these three states alongside the corresponding loss coefficients.

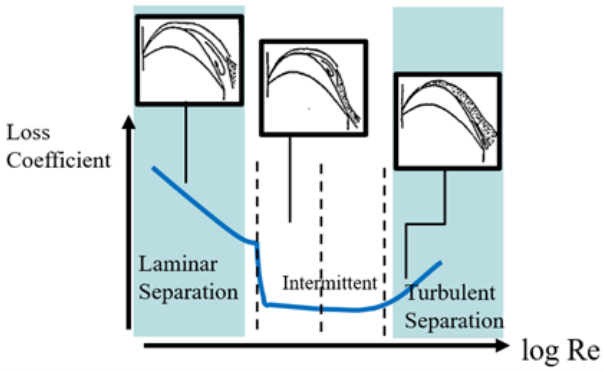

Figure 1: Loss Coefficient as a function of Reynolds in different type of separations [1].

Previous experimental studies on separated flows show that three instabilities appear in the separated region. The twp dominant instabilities are the Kelvin-Helmholtz (K-H) and shedding instabilities. The K-H and shedding instabilities are closely related, as both originate from shear layer instability. Experimental data show that the K-H instability scales with the momentum thickness [17, 18], while the shedding scales with the size of the vortices and the local velocity at separation [18]. The last instability manifests as the low-frequency flapping of the separated shear layer [19, 20]. Active flow control strategies using synthetic jets have proven promising for effectively controlling boundary layer separation [7, 18, 21, 22, 23]. Moreover, separation over the suction side of Low-Pressure Turbine (LPT) blades is more likely to occur during off-design conditions. Hence, implementing passive control may alter the optimal design conditions. The use of zero-net mass flux actuation is also considered more relevant than other methods since turbine blades often incorporate cooling channels for structural requirements.

Experimental studies on controlling separation with synthetic jets indicate that low-frequency actuation, associated with shear layer instability, is the most effective [7, 18, 23, 24]. Specifically, Sigurdson [18] presents a sensitivity map of drag reduction as a function of actuation frequencies. This map shows that the optimum frequency is 2 to 5 times the shedding frequency. Additionally, the proposed scaling for the shedding frequency is given as a function of the size of shedding vortices (h) and the separation velocity, with a Strouhal number $St_h = f_{shed}\, h/U_s \approx 0.07 - 0.08$. This empirical formulation for determining the shedding frequency has been problematic, as it depends on geometry configurations and flow conditions. In more chaotic flows, the shedding

instability can also be indistinguishable from other eddies in instantaneous data, making it difficult to measure the size accurately.

In this study, active flow control with synthetic jets in laminar and turbulent boundary layer separations is considered at identical low Reynolds numbers and subsonic Mach numbers. Direct Numerical Simulations (DNS) are performed using the high-order Discontinuous Galerkin spectral element solver, HORSES3D [25]. Figure 2 shows the laminar and turbulent separations over the bump geometry with steady inflow and no actuation. In the laminar boundary layer, the flow separates just upstream of the bump summit. The separated shear layer sustains a self-excited shedding of spanwise-dominant Kelvin-Helmholtz (K-H) vortices, followed by their breakdown into smaller three-dimensional structures and an abrupt transition to turbulence. The entrainment provided by turbulence leads to mean flow reattachment. In turbulent boundary settings, the separated shear layer breaks into smaller eddies sooner, generating more chaotic vortices without distinct K-H vortices. In both conditions, the shedding vortices are indistinguishable, making the estimation of the optimum frequency challenging.

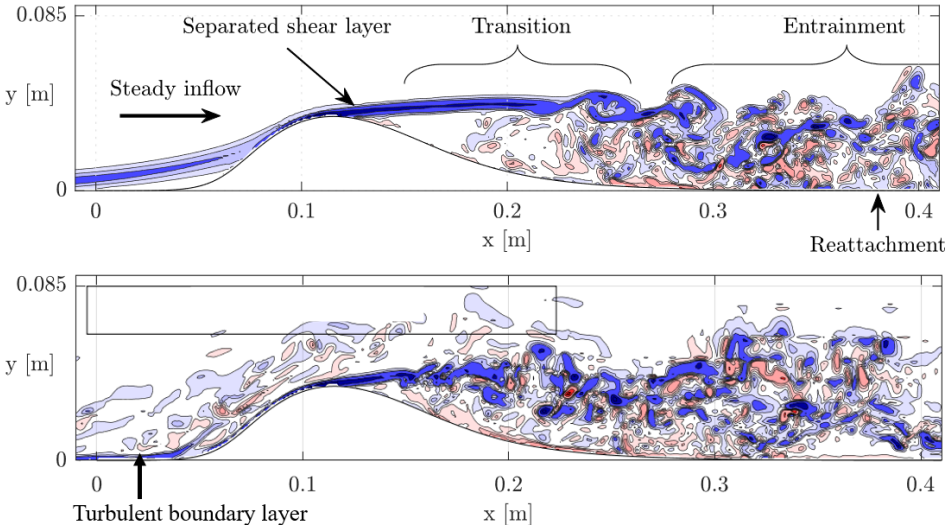

Figure 2: Instantaneous spanwise vorticity field around a wall-mounted bump under steady inflow conditions. Top: laminar boundary layer [16]; Bottom: turbulent boundary layer.

2 NUMERICAL SETUPS

2.1 Governing Equations

The numerical simulations solve the compressible Navier-Stokes equations without any turbulence wall modelling or known as Direct Numerical Simulation (DNS). The DNS simulations were done with the in-house discontinuous Galerkin spectral element code HORSES3D [25]. The flow variables are made dimensionless using L_{Ref}, T_{Ref}, p_{Ref} and the reference velocity U_{ref} for the steady inflow case, resulting in a unit-length Reynolds number Re =100 000 and Mach number 0.2. The dimensionless compressible Navier-Stokes equations in conservative form take the form

$$\frac{\partial \mathbf{q}}{\partial t} + \boldsymbol{\nabla} \cdot (\mathbf{f^a} - \mathbf{f^v}) = \mathbf{s}, \tag{1}$$

where $\mathbf{q} = [\rho,\ \rho u,\ \rho v,\ \rho w,\ \rho E]^T$ are the conservative variables, E is the specific internal energy and $\mathbf{s}$ is a source or volumetric forcing term. Advective ($\mathbf{f^a}$) and viscous ($\mathbf{f^v}$) fluxes are expressed in primitive variables as equations (2) and (3), respectively.

$$\mathbf{f}_1^a = \begin{bmatrix} \rho u \\ p + \rho u^2 \\ \rho uv \\ \rho uw \\ u(\rho E + p) \end{bmatrix}, \quad \mathbf{f}_2^a = \begin{bmatrix} \rho v \\ \rho uv \\ p + \rho v^2 \\ \rho vw \\ v(\rho E + p) \end{bmatrix}, \quad \mathbf{f}_3^a = \begin{bmatrix} \rho w \\ \rho uw \\ \rho vw \\ p + \rho w^2 \\ w(\rho E + p) \end{bmatrix}, \tag{2}$$

$$\mathbf{f}_1^v = \frac{1}{Re} \begin{bmatrix} 0 \\ \tau_{xx} \\ \tau_{xy} \\ \tau_{xz} \\ v_i \tau_{1i} + \kappa \partial_x T \end{bmatrix}, \quad \mathbf{f}_2^v = \frac{1}{Re} \begin{bmatrix} 0 \\ \tau_{yx} \\ \tau_{yy} \\ \tau_{yz} \\ v_i \tau_{2i} + \kappa \partial_y T \end{bmatrix}, \quad \mathbf{f}_3^v = \frac{1}{Re} \begin{bmatrix} 0 \\ \tau_{zx} \\ \tau_{zy} \\ \tau_{zz} \\ v_i \tau_{3i} + \kappa \partial_z T \end{bmatrix}, \tag{3}$$

The equation of state for ideal gas takes the form

$$p = (\gamma - 1)\, \rho \left[E - \frac{u^2 + v^2 + w^2}{2} \right], \tag{4}$$

and Sutherland's law is used for the dynamic viscosity

$$\mu = \frac{1 + T_{suth}/T_{Ref}}{T + T_{suth}/T_{Ref}} T^{\frac{3}{2}}, \tag{5}$$

where $T_{suth} = 110.4$ K. The dimensionless thermal conductivity is expressed as

$$\kappa = \frac{\mu}{(\gamma - 1)\, Pr\ M}, \tag{6}$$

where Pr is the Prandtl number, assumed to be constant and equal to 0.72. The stress tensor, using Stokes hypothesis, is defined as

$$\boldsymbol{\tau} = \mu \left((\nabla \boldsymbol{v})^T + \nabla \boldsymbol{v} \right) - \frac{2}{3} \mu \left(\boldsymbol{\nabla} \cdot \boldsymbol{v} \right)\ \boldsymbol{I} \tag{7}$$

The simulations are performed using 3rd-order polynomials with Gauss nodes. Time integration is performed with an explicit 3rd-order Runge-Kutta scheme. A standard discontinuous Galerkin discretization of the inviscid fluxes is done using Roe's method for the Riemann problem and the Bassi-Rebay 1 scheme is used for the discretization of the viscous fluxes.

2.2 Flow configuration

The study is performed with an extruded bump geometry (2.5D) inside a channel. This geometry is based on Saavedra's experiment [11]. This geometry is defined with a Bezier curve with 11 control points to ensure C1 and C2 continuity. The bump maximum height (summit) and the channel height are 0.036 m and 0.17 m, respectively, resulting in a throat width of 0.134 m and a blockage ratio of 21.2 %. This setup is given in Figure 3. The detail of the boundary conditions is given in Table 1 with the reference density is ρ_{Ref}=1.184kg/m3. This domain is discretised with high-order mesh into two meshes; 63,864 elements (laminar separation simulations) and 192,000 elements (turbulent separation simulations). Third order (3rd) polynomial is used in all simulations and results in 4,087,296 and 12,288,000 Degrees of Freedom (DOF) for the laminar and turbulent separation, respectively. A fringe is applied to prevent upstream contamination of the solution caused by reflections from the outlet. Convergence study of the mesh has been done considering h and p refinements, but is not discussed in this study [16]. The geometry and flow conditions are identical with previous study on the impact of oscillating inflow, see Marbona *et al.* [16].

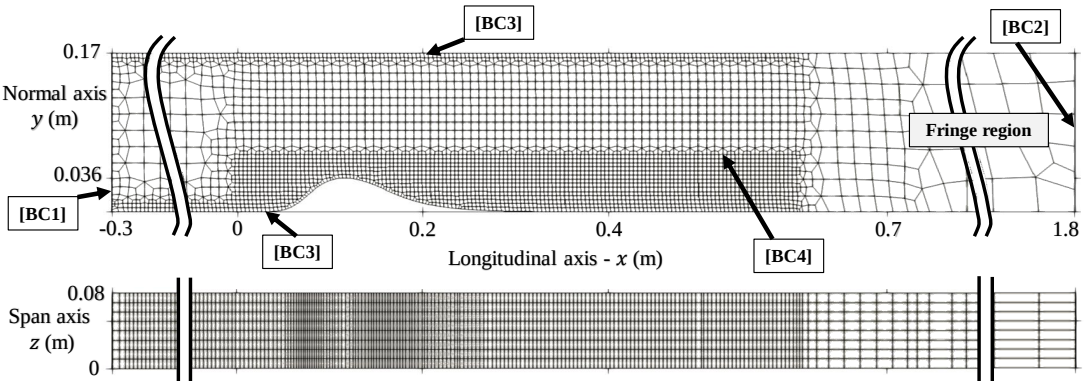

Figure 3: Computational domain and representative mesh for spectral element computations [16].

Table 1: Boundary Conditions

[BC1] Inlet	Total pressure p_t and total temperature $T_t = 291.2$ K
[BC2] Outlet	Static pressure: $p = 101\ 325$ Pa
[BC3] Wall	No-slip, adiabatic
[BC4] Sides	Periodicity
[BC5] Synthetic Jets	Oscillating Poiseuille boundary condition

Reference flow conditions are defined in which the inlet total pressure is constant and equal to $p_t = 105319$ Pa and the inlet total temperature is $T_t = 291.2$ K; this case is referred to as the laminar boundary with no actuation case. Under these conditions, the mean velocity at the inlet section is $U_{Ref} = 68.158$ m/s, and the static temperature at inflow (which is taken as reference temperature) is T_{Ref}= 288.9 K. The resulting flow has (unit length) Reynolds number

$Re = \rho_{Ref} U_{Ref} L_{Ref}/\mu_{Ref} \approx 100,000$ and Mach number $M = U_{Ref}/c_{Ref} = 0.2$, where ρ_{Ref}, μ_{Ref}, and c_{Ref} are respectively the density, dynamic viscosity and speed of sound based on the reference temperature and pressure (T_{Ref} and p_{Ref}=101325 Pa) and L_{Ref} is an arbitrary reference length which is chosen as $L_{Ref} = 1$ m. In these flow conditions, the laminar boundary layer separates around the bump summit. It creates a separated shear layer and experiences an abrupt transition process along with a self-excited shedding of spanwise-dominant KH vortices. The length of the streamwise distance of the separated region is $L_{(s,steady)} = 0.2782$ m. The Reynolds number is based on the length of the separated region $Re \approx 27,000$. Furthermore, the Reynolds number based on the momentum thickness of the boundary layer at separation is $Re_{(\theta,s)} = 27$. Turbulent boundary layer conditions are imposed using turbulent zero pressure gradient (ZPG) Poiseuille flow data as inflow. This data is obtained from an auxiliary simulation with identical cross-sectional dimensions to a turbulent plane Poiseuille flow under identical flow conditions.

2.3 Synthetic jet actuation

A synthetic jet is applied at a location from x=0.1025 m to x=0.1075 m and extended in the spanwise direction to induce a 2D disturbance. This location is just upstream of the separation point, as illustrated in Figure 4. Dirichlet boundary conditions are imposed using an oscillating Poiseuille solution, which ensures a zero-net mass flux and maintains a continuous streamwise velocity profile. The synthetic jet is ejected vertically and is described in detail by Eqs. (8), (9), and (10)[26].

$$v(x,t) = \frac{A_{jet}}{i\rho\omega_{jet}} \left\{ 1 - \frac{\cosh\left[\sqrt{\omega_{jet}/2\nu}\,(1+i)\,x\right]}{\cosh\left[\sqrt{\omega_{jet}/2\nu}\,(1+i)\,h_{jet}\right]} \right\} \tag{8}$$

$$u(x,t) = w(x,t) = 0 \tag{9}$$

$$p(x,t) = \bar{p}(x)_{no\ jet} \tag{10}$$

where A_{jet} is the amplitude of the synthetic jet velocity relative to the reference velocity $A_{jet} = U_{jet}/U_{Ref}$, ω_{jet} is the frequency of actuation $\omega_{jet} = 2\pi f^*_{jet}$, $f^*_{jet} = f_{jet}\ L_{Ref}/U_{Ref}$ is the dimensionless frequency of the actuation, $t^* = tU_{Ref}/L_{Ref}$ is a dimensionless time and t^*_0 is a reference instant.

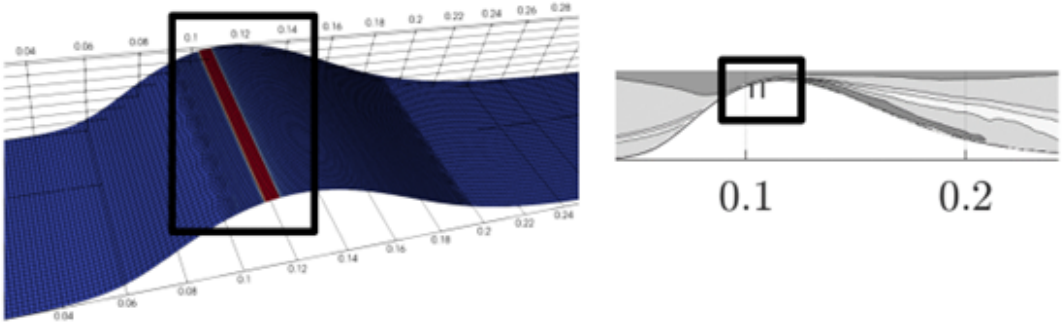

Figure 4: Location of synthetic jet boundary condition – oscillating Poiseuille .

2.4 Mode decomposition

A data-driven decomposition method has been developed to distinguish organized large-scale dynamics from chaotic ones. The method originates from the Hilbert transform and decomposes signals into their components based on frequency bandwidth. Equation (11) expresses this generalized idea using wavelet transform filtering.

$$\tilde{X}(l,t',\theta) = \int_{-\infty}^{\infty} \hat{X}(k)\hat{\psi}^*_{l,t',\theta}(k)dk \tag{11}$$

The wavelet transform filtering decomposes the spatiotemporal data by frequency binning of the temporal component to obtain the temporal coefficient. The spatial mode is the residual function, which, when multiplied by the temporal coefficient, forms the spatiotemporal mode. The decomposition has been implemented in the study and can distinguish the most dominant modes in the instantaneous flow field. Figures 5 and 6 depict the Kelvin-Helmholtz and the bubble shedding identified through the decomposition, respectively. Each instability is characterized by its spatial structure of the streamwise velocity component, R(u), and normal, R(v), velocity component. The normalized frequency of the shedding in the laminar separation case, f^*_{shed}, is 2.8. In the turbulent boundary layer setup, this frequency is 2.5.

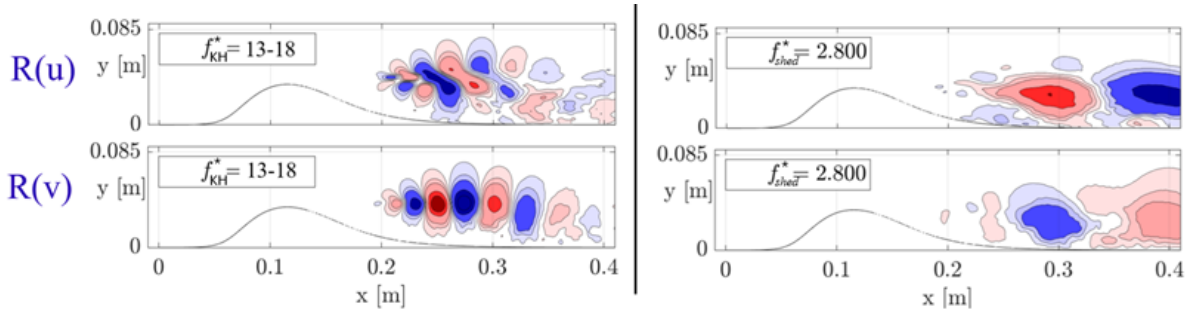

Figure 5: Two dominant instabilities: KH (left) and shedding (right) instability with its corresponding frequency for laminar boundary layer separation over the bump without actuation.

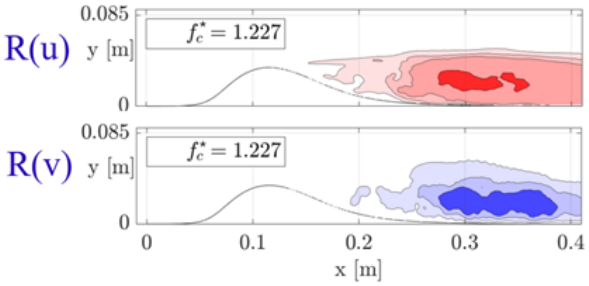

Figure 6: Low frequency flapping with its corresponding frequency for laminar boundary layer separation over the bump without actuation.

Table 2: Summary of the cases simulated, including the amplitude and frequency of jet actuation, and its frequency ratio to the shedding frequency f^*_{shed}. The location of mean separation and reattachment are given along with the length of recirculation region L_s and the relative reduction to the unforced case ΔL_s.

Case	Boundary layer	A_{jet}	f^*_{jet}	f^*_{jet}/f^*_{shed}	x_s (m)	x_r (m)	L_s (m)	ΔL_s (m)
No actuation	laminar	-	-	-	0.11	0.3866	0.2782	-
	turbulent	-	-	-	0.1149	0.4065	0.2917	-
Actuation	laminar	0.04	2	0.71	0.1156	0.3626	0.2470	-0.0312
		0.04	15	5.4	0.1180	0.2633	0.1453	-0.0680
Actuation	laminar	0.2	2	0.7	0.1184	0.3384	0.2199	-0.0583
		0.2	8	2.9	0.1174	0.2912	0.1738	-0.1044
		0.2	12	4.3	0.1178	0.2701	0.1523	-0.1259
		0.2	15	5.4	0.1180	0.2633	0.1453	-0.1329
		0.2	16	5.7	0.1173	0.2598	0.1424	-0.1358
		0.2	20	7.1	0.1092	0.2946	0.1854	-0.0928
Actuation	turbulent	0.2	2	0.8	0.1193	0.3554	0.2361	-0.0555
		0.2	15	6	0.1190	0.290	0.1718	-0.1198

3 RESULTS

Table 2 presents the DNS simulations performed with different setups. The twelve simulations include two cases without actuation for each boundary layer condition and ten cases with synthetic jet actuation. In the laminar boundary layer condition, two actuation amplitudes, 0.04 and 0.2, are implemented. These magnitudes are consistent with those in Kiya's experimental study [24]. The dimensionless frequency of actuation ranges from 2 to 15, approximately 0.7 to 7 times the frequency of shedding. Note that the low frequency of 2 corresponds to the large vortex cluster as in [16], while the high frequencies aim at the Kelvin-Helmholtz. For each case, the corresponding separation and reattachment locations are provided. The length of the separation region is then calculated by subtracting these two values. The separation and reattachment regions are determined from the zero value of skin friction in the mean flow field, temporal and spanwise average. In the actuation cases, the reduction in the separation region is given relative to the no-actuation case of the corresponding boundary layer condition. In Table 3, the reduction percentage is also provided relative to the no-actuation case and the maximum reduction of each setup.

Without the synthetic jets, the difference between the separation regions of the laminar and turbulent boundary layers is identifiable. The turbulent boundary layer separates and reattaches further downstream than the laminar one, producing a slightly longer recirculation region overall. The time-averaged streamwise velocity flow field provides better insight into the recirculation region, as presented in Figure 7. The locations of separation and reattachment can be estimated

Table 3: Percentage of reduction in the recirculation relative to the unforced case.

Case	Boundary layer	A_{jet}	f^*_{jet}	f^*_{jet}/f^*_{shed}	$\Delta L_s/(L_s)_{no\ jet}$ (%)	$\Delta L_s/(\Delta L_s)_{max}$ (%)
Actuation	laminar	0.04	2	0.71	-11.2	-45.9
		0.04	15	5.4	-24.5	-100
Actuation	laminar	0.2	2	0.7	-20.9	-42.9
		0.2	8	2.9	-37.5	-76.9
		0.2	12	4.3	-45.2	-92.7
		0.2	15	5.4	-47.8	-97.9
		0.2	16	5.7	-48.8	-100
		0.2	20	7.1	-33.3	-68.3
Actuation	turbulent	0.2	2	0.8	-19.0	-46.3
		0.2	15	6	-41.1	-100

from the zero-value streamwise velocity on the surface. In the laminar settings, a significant portion of the 'dead air' region exists after separation, indicating a pressure plateau on the surface and a long bubble. For the turbulent conditions, there is no 'dead air' region, and the separated region is pushed towards the surface.

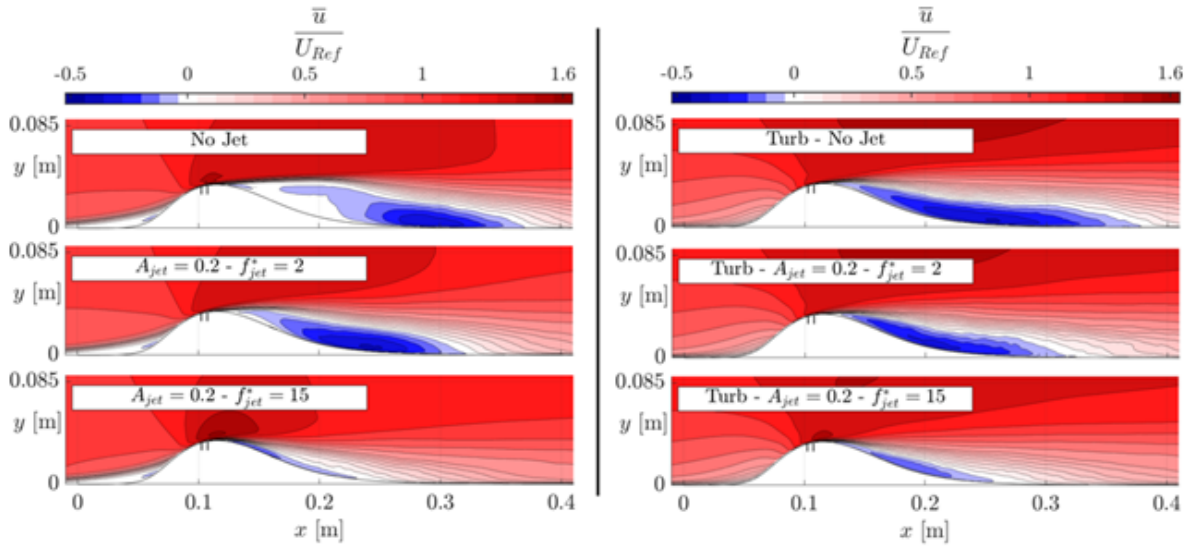

Figure 7: Time average streamwise velocity. Left: laminar boundary layer; Right: turbulent boundary layer.

In the cases with actuation, the introduction of disturbance just upstream of the separation location pushes the separation region slightly more downstream in a nonlinear manner. It

also affects the reattachment location non-linearly, reducing the recirculation region for the tested amplitude and frequency range. The disturbance reduces the 'dead air' region in the mean flow field, promoting an earlier entrainment process. The maximum reduction occurs around a dimensionless actuation frequency of 15-16. These values correspond to 5.4 and 5.7 for the laminar separation with an amplitude of 0.2, accounting for a $48-49\%$ reduction in the separation region, respectively. For the same amplitude but with turbulent conditions, the maximum reduction measured is 42% relative to the no-actuation cases with turbulent conditions.

Sensitivity maps are created to better locate the optimum frequency of actuation. Figure 8 shows the map relative to the no-actuation cases. In the laminar boundary layer, the effect of amplitude on the reduction appears to have a logarithmic relationship, which aligns with Kiya's experimental study[24]. Moreover, the maximum reduction measured closely mirrors the outcomes of that study. Figure 9 presents the map relative to the maximum reduction observed for each amplitude and boundary layer condition. The results condense into a similar trend for all setups and show good agreement with Sigurdson's study [18]. The optimum frequency for maximum reduction in the recirculation region is 5 to 6 times the frequency of shedding.

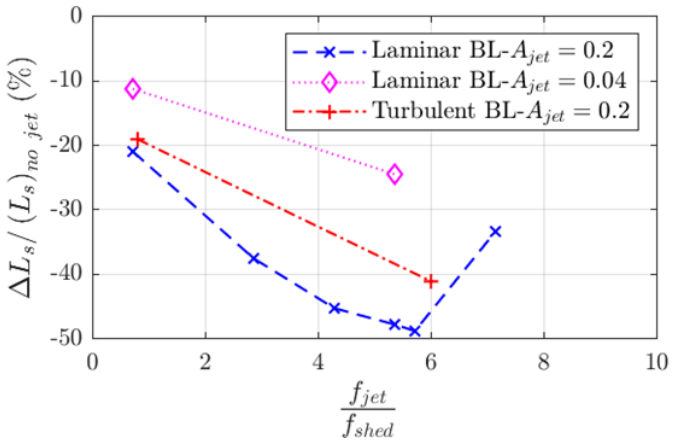

Figure 8: Sensitivity map of optimum actuation frequency and the corresponding reduction in separation length at different jet amplitude and boundary layer condition.

Figures 10 and 11 depict the instantaneous spanwise vorticity fields in the actuation cases with amplitude 0.2 and frequencies of 2 and 15, respectively. Laminar and turbulent separation cases are compared at identical jet phases. In the laminar separation case at a frequency of 2, periodic generation of a large vortex cluster comprising smaller vortices occurs, pulling the fluid together in the recirculation region, akin to those induced by inflow fluctuations [16]. In contrast, the turbulent setup shows a diffuse artifact of the vortex cluster with smaller eddies. At an actuation frequency of 15, different observations emerge. For the laminar separation case, a dominant spanwise vortex forms from the synthetic jet's interaction with the separated shear layer, traveling downstream near the bump's surface and amalgamating with other vortices. For the turbulent separation case, such vortices are less visible, suggesting either earlier amalgamation or alternative mechanisms at work.

Figure 12 presents the spatial structure of vertical velocity in the most energetic mode for the

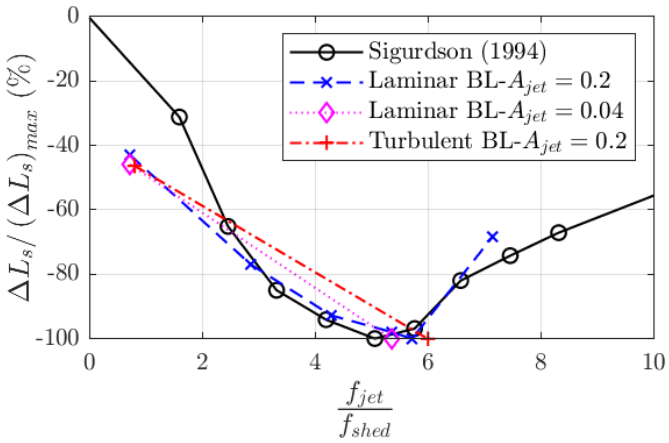

Figure 9: Sensitivity map of optimum actuation frequency and the corresponding reduction in separation length relative to the maximum reduction at different jet amplitude and boundary layer condition.

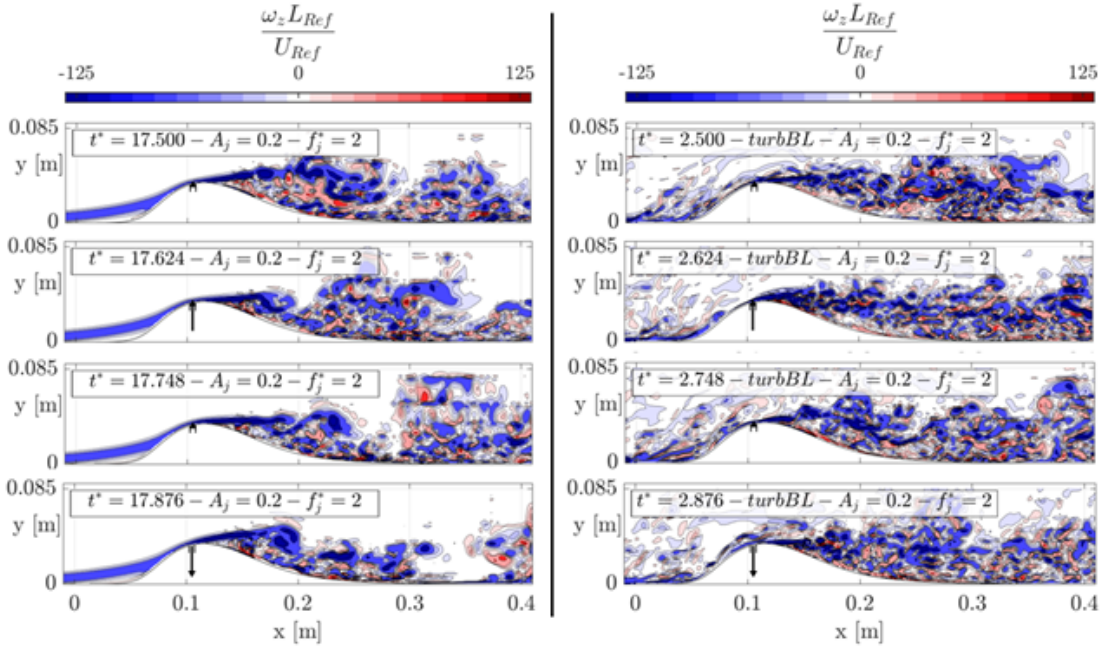

Figure 10: Instantaneous spanwise vorticity with A_{jet}=0.2 and f^*_{jet}=2. Left: laminar boundary layer; Right: turbulent boundary layer. The jet actuation phase from top to bottom: 0°, 90°, 180°, and 270°. The arrows indicate the state of the jet velocity.

actuation cases. Two scenarios are depicted, both with an amplitude of 0.2, but with frequencies of 2 and 15. Under laminar boundary layer conditions, the dominant mode at low actuation frequencies exhibits a frequency higher than the actuation frequency, which is indicative of the vortex cluster mechanism. The occurrence of a frequency higher than the actuation frequency suggests that this mechanism does not manifest uniformly across all phases, consistent with the findings of Marbona *et al.* [16]. At high actuation frequencies in laminar conditions, the

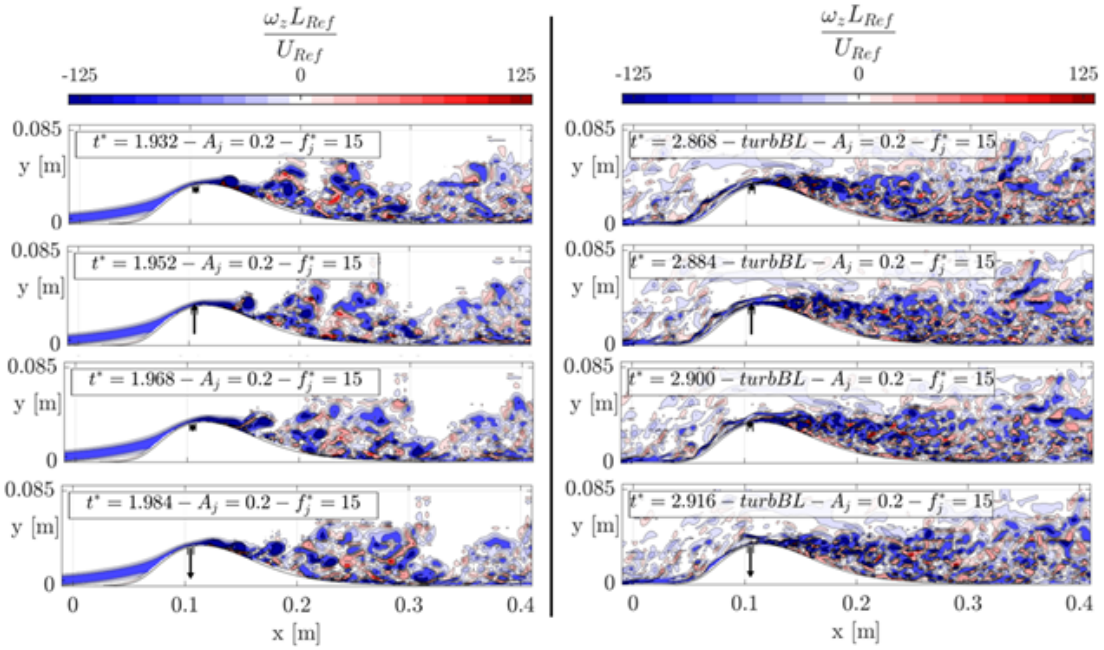

Figure 11: Instantaneous spanwise vorticity with A_{jet}=0.2 and f^*_{jet}=15. Left: laminar boundary layer; Right: turbulent boundary layer. The jet actuation phase from top to bottom: 0°, 90°, 180°, and 270°. The arrows indicate the state of the jet velocity.

dominant mode involves vortices generated by the interaction with the separated shear layer, promoting the Kelvin-Helmholtz vortices. In turbulent boundary conditions, the dominant mode is observed at a dimensionless frequency between 1.7 and 1.9, indicating that it is likely not influenced by the synthetic jet frequency.

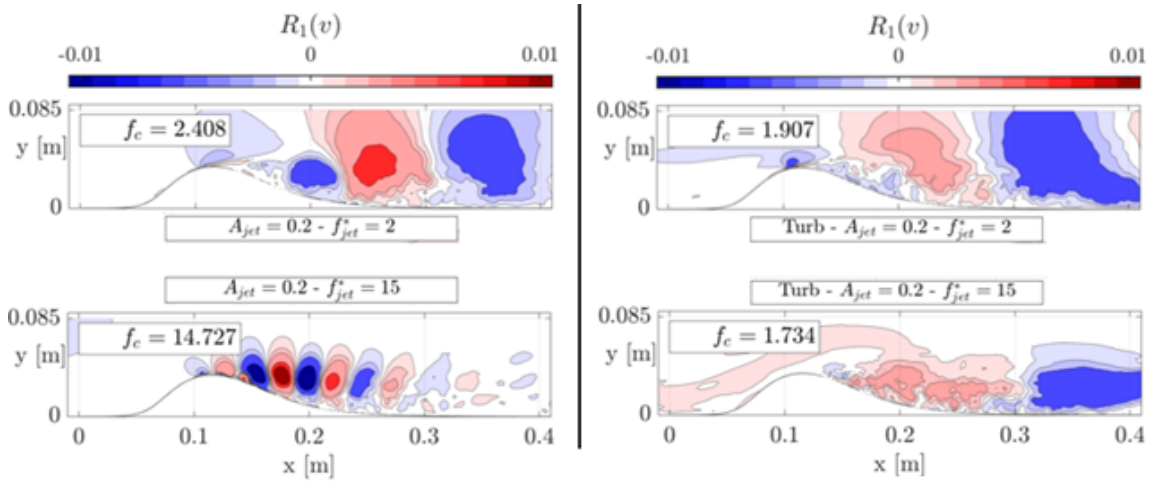

Figure 12: The spatial structure of vertical velocity in the most energetic mode for actuation cases. Top: A_{jet}=0.2 and f^*_{jet}=2; Bottom: A_{jet}=0.2 and f^*_{jet}=15. Left: laminar boundary layer; Right: turbulent boundary layer.

Figure 13 depicts the mean flow field of turbulence kinetic energy (TKE). According to Sigurdson [18] and Dandois *et al.* [23], there is a correlation between the reduction of the separated flow region and an increase in TKE, which enhances the entrainment process. From the figure, this relationship appears evident at low actuation frequencies. However, from the optimal actuation frequency, the proximity of high TKE areas to the surface and separation location seem more critical than their overall size.

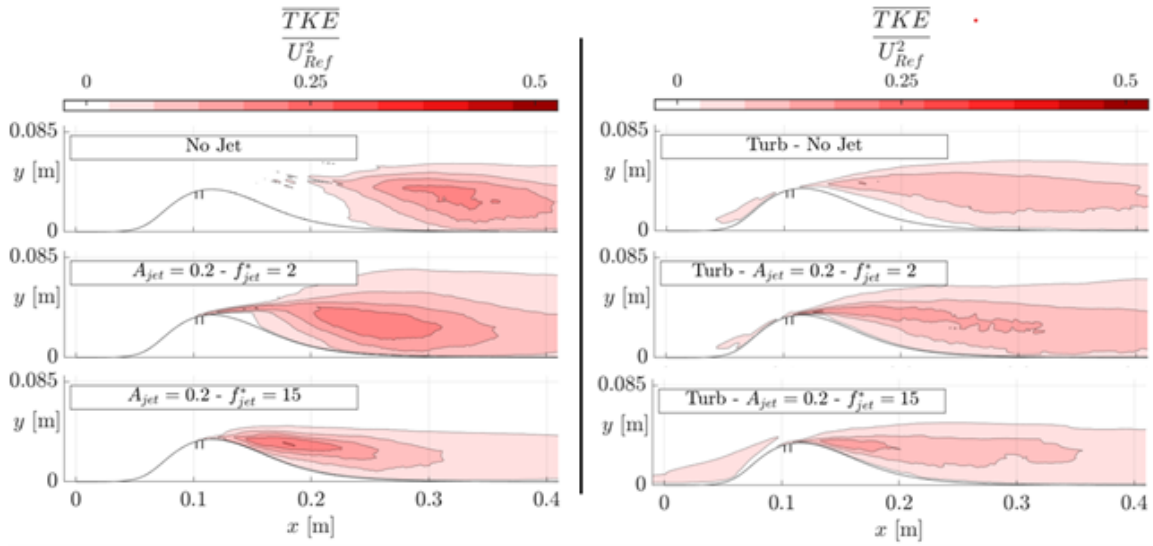

Figure 13: Time average turbulence kinetic energy (TKE). Left: laminar boundary layer; Right: turbulent boundary layer.

4 CONCLUSIONS

Active control of separated flow is studied at both low and high frequencies, with the goal of promoting Kelvin-Helmholtz instabilities at high frequencies and large vortex clusters at low frequencies, as described in [16]. Cases with laminar and turbulent incoming boundary layers are considered. The findings reveal that the most efficient strategy involves energizing the KH vortices, as even a weak forcing amplitude is sufficient to shorten the recirculation region. In contrast, low-frequency actuation in the laminar boundary layer can promote the formation of large vortex clusters but requires stronger forcing and is less effective overall.

Sensitivity maps are constructed at different forcing frequencies to determine the optimal actuation frequency. These maps show good agreement with the findings from Sigurdson's study on both laminar and turbulent boundary layer separations. The optimal actuation frequency is estimated to be between 5 to 6 times the shedding frequency (f_{shed}). Although this physical phenomenon persists in chaotic turbulent flows, it can be difficult to distinguish from other features in the instantaneous flow field. A data-driven decomposition method is used to analyze the chaotic flow and identify its dominant modes, allowing for the precise determination of the optimal frequency. This approach helps to establish the optimal forcing frequency for various geometric configurations and flow conditions.

ACKNOWLEDGEMENTS

This project has received funding from the European Union's Horizon 2020 research and innovation programme under the Marie Skłodowska Curie grant agreements No 955923-SSECOID and 101019137-FLOWCID. D.R. and H.M. also acknowledge funding by the Government of the Community of Madrid within the multi-annual agreement with Universidad Politécnica de Madrid through the Program of Excellence in Faculty (V-PRICIT line 3). The authors gratefully acknowledge the Universidad Politécnica de Madrid (www.upm.es) for providing computing resources on Magerit Supercomputer.

REFERENCES

[1] J. Hourmouziadis, "Aerodynamic design of low pressure turbines," in AGARD Lecture Series, vol. 167, AGARD, 1989, pp. 8.1–8.40.

[2] R. E. Mayle, "The 1991 IGTI Scholar Lecture: The Role of Laminar-Turbulent Transition in Gas Turbine Engines," Journal of Turbomachinery, vol. 113, pp. 509, 1991. https://doi.org/10.1115/1.2929110

[3] J. P. Bons, R. Sondergaard, and R. B. Rivir, "The Fluid Dynamics of LPT Blade Separation Control Using Pulsed Jets," Journal of Turbomachinery, vol. 124, pp. 77, 2002. https://doi.org/10.1115/1.1425392

[4] J. D. Coull and H. P. Hodson, "Unsteady boundary-layer transition in low-pressure turbines," Journal of Fluid Mechanics, vol. 681, pp. 370, 2011. https://doi.org/10.1017/jfm.2011.204

[5] D. Greenblatt and I. J. Wygnanski, "The control of flow separation by periodic excitation," Progress in Aerospace Sciences, vol. 36, pp. 487, 2000. https://doi.org/10.1016/S0376-0421(00)00008-7

[6] R. J. Volino, O. Kartuzova, and M. B. Ibrahim, "Separation Control on a Very High Lift Low Pressure Turbine Airfoil Using Pulsed Vortex Generator Jets," Journal of Turbomachinery, vol. 133, 2011. https://doi.org/10.1115/1.4003024

[7] D. Postl, W. Balzer, and H. F. Fasel, "Control of laminar separation using pulsed vortex generator jets: direct numerical simulations," Journal of Fluid Mechanics, vol. 676, pp. 81–109, 2011. https://10.1017/jfm.2011.34

[8] D. Rodríguez, E. M. Gennaro, and L. F. Souza, "Self-excited primary and secondary instability of laminar separation bubbles," J. Fluid Mech. 906, A13, 2021. https://10.1017/jfm.2020.767

[9] A. Seifert and L. G. Pack, "Active flow separation control on wall-mounted hump at high Reynolds numbers," AIAA Journal, vol. 40, pp. 1363, 2002. https://doi.org/10.2514/2.1796

[10] D. Greenblatt, K. B. Paschal, C.-S. Yao, J. Harris, N. W. Schaeffer, and A. E. Washburn, "Experimental investigation of separation control Part 1: Baseline and steady suction," AIAA Journal, vol. 44, pp. 2820, 2006. https://doi.org/10.2514/1.13817

[11] J. Saavedra and G. Paniagua, "Transient Performance of Separated Flows: Characterization and Active Flow Control," Journal of Engineering for Gas Turbines and Power, vol. 141, no. 10.1115/1.4040685, 2018, 011002. https://doi.org/10.1115/1.4040685

[12] R. Balin and K. Jansen, "Direct numerical simulation of a turbulent boundary layer over a bump with strong pressure gradients," Journal of Fluid Mechanics, vol. 918, A14, https://2021.10.1017/jfm.2021.312

[13] A. Uzun and M. R. Malik, "High-fidelity simulation of turbulent flow past Gaussian bump," AIAA Journal, vol. 60, pp. 2130, 2022. https://10.2514/1.J060760

[14] H. D. Nowak, F. Lluesma-Rodriguez, I. Rahbari, J. P. Clark, and G. Paniagua, "Response of Separated Boundary Layers to Steady and Pulsated Flow Injection," Journal of Turbomachinery, vol. 145, no. 10.1115/1.4056184, 2022, 061001. https://10.1115/1.4056184

[15] A. Prakash, R. Balin, J. A. Evans, and K. E. Jansen, "A streamline coordinate analysis of a turbulent boundary layer subject to pressure gradients and curvature on the windward side of a bump," Journal of Fluid Mechanics, vol. 984, A23, 2024. https://10.1017/jfm.2024.199

[16] H. Marbona, D. Rodríguez, A. Martínez-Cava, and E. Valero, "Impact of harmonic inflow variations on the size and dynamics of the separated flow over a bump," Physical Review Fluids, vol. 9, 053901, 2024. https://10.1103/PhysRevFluids.9.053901

[17] M. A. Z. Hasan, "The flow over a backward-facing step under controlled perturbation: laminar separation," Journal of Fluid Mechanics, vol. 238, pp. 73–96, 1992. https://10.1017/S0022112092001642

[18] L. W. Sigurdson, "The structure and control of a turbulent reattaching flow," Journal of Fluid Mechanics, vol. 298, pp. 139–165, 1995. https://10.1017/S0022112095003259

[19] J. K. Eaton and J. P. Johnston, "A review of research on subsonic turbulent flow reattachment," AIAA Journal, vol. 19, pp. 1093, 1981. https://10.2514/3.60048

[20] X. Fang and Z. Wang, "On the low-frequency flapping motion in flow separation," Journal of Fluid Mechanics, vol. 984, A76, 2024. https://10.1017/jfm.2024.280

[21] A. Seifert, T. Bachar, D. Koss, M. Shepshelovich, and I. Wygnanski, "Oscillatory blowing: A tool to delay boundary-layer separation," AIAA Journal, vol. 31, pp. 2052, 1993. https://10.2514/3.49121

[22] D. Greenblatt, K. B. Paschal, C.-S. Yao, and J. Harris, "Experimental investigation of separation control part 2: Zero mass-flux oscillatory blowing," AIAA Journal, vol. 44, pp. 2831, 2006. https://10.2514/1.19324

[23] J. Dandois, E. Garnier, and P. Sagaut, "Numerical simulation of active separation control by a synthetic jet," Journal of Fluid Mechanics, vol. 574, pp. 25–58, 2007. https://10.1017/S0022112006003995

[24] M. Kiya, M. Shimizu, and O. Mochizuki, "Sinusoidal forcing of a turbulent separation bubble," Journal of Fluid Mechanics, vol. 342, pp. 119–139, 1997. https://10.1017/10.1017/S0022112097005521

[25] E. Ferrer, G. Rubio, G. Ntoukas, W. Laskowski, O. Mariño, S. Colombo, A. Mateo-Gabín, H. Marbona, F. Manrique de Lara, D. Huergo, J. Manzanero, A. Rueda-Ramírez, D. Kopriva, and E. Valero, "HORSES3D: A high-order discontinuous Galerkin solver for flow simulations and multi-physics applications," Computer Physics Communications, 108700, https://doi.org/10.1016/j.cpc.2023.108700, 2023. https://doi.org/10.1016/j.cpc.2023.108700

[26] H.-L. Ma and C.-H. Kuo, "Theoretical analysis of an oscillatory plane Poiseuille flow—A link to the design of vortex flow meter," Physics of Fluids, vol. 29, 053602, 2017. https://doi.org/10.1063/1.4984006